Mechanically driven wrinkling instability in thin film polymer bilayers

J. S. Sharp,* K. R. Thomas, and M. P. Weir
School of Physics and Astronomy, University of Nottingham, Nottingham, NG7 2RD, United Kingdom
(Received 20 July 2006; revised manuscript received 15 September 2006; published 3 January 2007)

Optical microscopy and atomic force microscopy were used to study a mechanically induced wrinkling instability in thin film poly(caprolactone)/polystyrene and poly(ethylene oxide)/poly(methyl methacrylate) bilayers. The instability in these samples was shown to be driven by changes in the interfacial area between a semicrystalline polymer underlayer and a glassy polymer capping layer that occurred when the underlayers were melted. The wrinkling instability resulted in the formation of one-dimensional corrugations at the surface of the bilayer samples that had a well-defined wavelength on the micrometer length scale. A linear stability analysis was used to derive a simple model of the wrinkling process in these samples. This model considered the flow and deformation of material in the molten underlayer as well as the balance of stresses in the glassy polymer capping layers. Rheological data were also obtained from polymers similar to those used to form the bilayers. These data were used to show that the model is capable of quantitatively predicting the capping layer and underlayer thickness dependencies of the characteristic wrinkling wavelengths, if the mechanical properties of the two layers and the strain in the capping layers can be determined.

DOI: 10.1103/PhysRevE.75.011601 PACS number(s): 68.55.−a, 61.41.+e, 68.35.Ct, 68.35.Ja

I. INTRODUCTION

Pattern formation and pattern replication techniques are becoming increasingly attractive as methods of producing topographic surface structures on the submicrometer to micrometer length scale. These methods usually involve the use of optical lithography [1,2] or soft lithography based techniques [1] and have a wide range of applications in engineering, biology, and tissue engineering [1–3]. However, a major disadvantage of using these methods is that they often require the manufacture of a mask to perform the pattern transfer. This requires the production of preexisting structures on the mask that are similar in size to the structures that are to be reproduced on the surfaces of interest. A more attractive method of patterning surfaces with well-controlled topographical structures is to use competing thin film physical processes that result in the formation of structures on a well-defined characteristic length scale. These so called *kinetic length scale selection processes* occur as the result of the competition between two or more physical processes that favor structure formation on different length scales (long and short). Examples of these processes include spinodal dewetting in thin liquid films [4], dispersion driven morphologies in polymer/inorganic multilayer structures [5], and electric-field-induced instabilities in thin dielectric films [6]. One disadvantage of using these processes to produce patterned surfaces is that the structures that form are often transient and will continue to evolve and coarsen toward a structureless state. However, the use of polymeric materials as one or more of the layers in these systems can help to overcome these difficulties. The ability to rapidly recrystallize one of the layers or quench a polymer through a dynamic glass transition can be used to "freeze-in" these transient structures.

A particular class of process that exploits these pattern formation methods involves the use of thin film mechanical instabilities to buckle the surface of polymer/polymer or polymer/inorganic multilayer structures. These methods usually result in the production of structures with characteristic lateral feature sizes on the micrometer length scale and often exploit the differential response of the layers in the system to a change in temperature [7–9], an applied mechanical stress, or a swelling solvent [10,11]. This differential response results in one or more of the layers in the system being left in a state of compressive stress when the samples are heated, deformed, or immersed in solvent. The stresses that arise in these samples can then cause the layered system to buckle. However, the adhesion between the different layers often places additional constraints on the system and prevents the samples from buckling with the lowest energy bending mode (i.e., with a wavelength comparable to the lateral dimensions of the sample). As a result of this, the system tends to select a characteristic buckling/wrinkling wavelength that acts as a compromise between the compressive stresses that are introduced initially and the bending stresses that arise in the buckled state [12]. A number of theoretical models have been developed to try to predict the length scales that are associated with the wrinkling patterns observed in thin elastic layers supported on elastic [7,12,13], viscous [14,15], and viscoelastic substrates [13,16,17].

In this paper, we describe a study of a mechanically driven wrinkling instability in thin film polymer/polymer bilayers comprising a semicrystalline polymer underlayer and a glassy polymer capping layer. The wrinkling instability in this system is shown to be driven by changes in the interfacial area between the underlayer and the capping layer that occur when the underlayers are melted. The change in area of the interface between the two layers leaves the capping layer in a state of compressive stress and causes it to wrinkle.

This work expands upon the results of our previous study on a similar wrinkling instability in thin film poly(ethylene oxide)/polystyrene bilayers [17]. The present study considers the effects of changing the mechanical properties and thickness of the layers in the system and how these influence the resulting length scales associated with the morphologies that

*Email address: james.sharp@nottingham.ac.uk

are observed at the surfaces of the bilayers. We show that the characteristic initial wrinkling length scale in these samples is sensitive to both the thickness and material properties of the polymer films that are used to manufacture these samples. An analytical expression based upon a simple linear stability analysis of the wrinkling process is derived for the wave-vector-dependent growth rates of height fluctuations at the surface of the bilayers. This simple model considers the flow of material in the molten viscoelastic underlayers and the balance of stresses that are exerted on the glassy capping layers. The theory is shown to quantitatively predict the dominant wrinkling length scale in the bilayer systems studied providing that the thickness and mechanical properties of the different layers and the mechanical strains in the capping layers can be determined.

II. EXPERIMENT

Thin film bilayers of poly(caprolactone) and polystyrene were prepared on 1 cm $\times$ 1 cm single-crystal silicon (Si) wafers ([100] orientation, Compart Technology). First, thin films of poly(caprolactone) (PCap, $M_w = 13\,000$ gmol^{-1}, $M_w/M_n = 1.18$, Polymer Source) were prepared by spin coating the polymer on the Si wafers from solutions in chloroform at 2000 rpm. The PCap films were then annealed on a Linkam microscopy hot stage at 60 °C [melting temperature T_m(PCap) = 58 ± 1 °C] for 2 min to remove excess solvent and to relax residual stresses introduced by the spin-coating procedure. The thickness of the films was controlled by varying the initial concentration of the solutions and was measured using a home-built self-nulling ellipsometer. The thickness of the PCap films was determined by mounting the samples on a Linkam microscopy hot stage and attaching them to the ellipsometer sample stage. The samples were then heated to 60 °C where the ellipsometric angles (P and A) required to obtain a null in the intensity of light reflected from the samples were recorded. These values of P and A were then used to determine the thickness and refractive index ($n = 1.506 \pm 0.002$) for the PCap films by assuming an isotropic semi-infinite slab model [18]. All of the ellipsometry measurements were performed using a HeNe laser (wavelength 633 nm) and at an angle of incidence of 60 ± 0.1°. Poly(caprolactone) films with thicknesses in the range 67–637 nm were prepared using this method. When the values of P_{null} and A_{null} had been determined, the samples were removed from the hot stage and allowed to recrystallize at room temperature.

Polystyrene (PS, $M_w = 654\,000$ gmol^{-1}, $M_w/M_n = 1.09$, Polymer Source) capping layers were then prepared by spin coating the polymer onto precleaned glass slides from solutions in toluene at 3000 rpm. The thickness of the PS films was controlled by varying the initial concentration of the solutions. The PS films were then cut around the edge of the glass slide using a scalpel and gently transferred onto a clean deionized water surface (Elga) using a film transfer technique described elsewhere [17,19]. A long thin metal support with a 15 mm diameter hole at one end was then used to pick the PS film up off the surface of the deionized water to produce a free-standing membrane of the polymer. This free-standing membrane was then annealed over a hotplate at ~100 °C [T_g(PS) = 97 ± 1 °C [20]] to remove wrinkles introduced by the water transfer technique and to tighten the membrane on the holder. At this stage in the process, great care was taken to avoid annealing the PS membranes for prolonged periods of time, as this prevented the rupture of the unsupported films under the action of dispersion forces between the two surfaces of the membranes. The PS membranes were then gently lowered onto the surface of the semicrystalline PCap layers supported on the Si wafers [see Figs. 1(a) and 1(b)]. At the point where the PS membranes contacted the PCap layers, surface forces pulled the two layers into intimate contact [Fig. 1(c)]. At this stage, a contact line developed at the polymer/polymer/air interface where the two films came into contact. As the films were pulled together, this contact line propagated from one side of the sample to the other. This had the effect of squeezing all the air from between the two polymer films and resulted in the production of a sharp interface between the two layers. This procedure was used to produce flawless bilayer samples using different combinations of the PCap and PS film thickness. The PS film thickness and refractive index were determined independently by transferring part of the same PS film

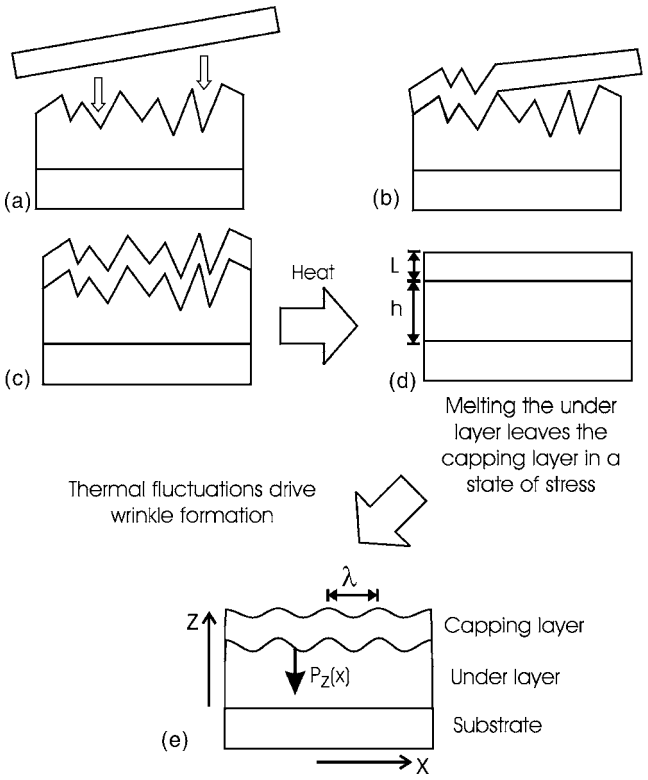

FIG. 1. Schematic diagram showing how the thin film bilayer samples are prepared. Thin film membranes of a glassy polymer are transferred onto the surface of a semicrystalline polymer film supported on a Si substrate (a). As the films are brought together, surface forces pull the two films into intimate contact [(b) and (c)]. When the bilayers are heated above the melting temperature of the underlayer, the interface between the two films is pulled flat by interfacial tension and the capping layer is left in a state of compressive stress (d). Thermal fluctuations at the surface of the bilayer then cause the capping layer to buckle (e).

that was used to produce each bilayer sample onto the metal holder described above. These PS films were then annealed above a hotplate and then gently lowered onto a clean Si wafer. The thickness and refractive index ($n=1.595\pm0.002$) of these substrate supported PS films were then measured using ellipsometry. Thin PS capping layers with thicknesses in the range 47–367 nm were produced using this method.

A second set of polymer bilayer samples was also prepared. Thin films of poly(ethylene oxide) (PEO, $M_w=32\,500$ gmol^{-1}, $M_w/M_n=1.09$, Polymer Source) were prepared by spin coating the polymer onto single-crystal Si wafers from solutions in chloroform at 2000 rpm. The thickness of the PEO films was varied by changing the initial concentration of the solutions used. These samples were then annealed on a Linkam hot stage at 65 °C [T_m(PEO)=63 °C] for 2 min. Ellipsometry measurements were then used to determine the thickness and refractive index ($n=1.495\pm0.005$) of the PEO films at a temperature of 70 °C using a similar procedure to that described above for the PCap films. Following film thickness determination, the PEO films were removed from the hot stage, cooled to room temperature, and allowed to recrystallize. Thin film capping layers of poly(methyl methacrylate) (PMMA, $M_w=838\,100$ gmol^{-1}, $M_w/M_n=1.57$, Polymer Source) were prepared by spin coating the polymer onto precleaned glass slides from solutions in toluene at 3000 rpm. The thickness was again varied by changing the initial concentration of the solutions used. The PMMA films were then cut and floated onto a clean deionized water surface, before being picked up on the metal holder to produce a free-standing membrane. These PMMA membranes were then annealed above a hotplate at ~110 °C [T_g(PMMA)=107 °C, [20]] to remove any wrinkles and they were then lowered gently onto the PEO films that were supported on the Si wafers. The thickness and refractive index ($n=1.490\pm0.005$) of the PMMA layers were determined using ellipsometry after similar PMMA films to those that were used to form the bilayers had been transferred from a water surface onto a clean Si wafer. PMMA capping layers with thicknesses in the range 49–278 nm were produced using this method.

Prior to the formation of the bilayers, the PCap and PEO films were inspected using an Olympus BX51 optical microscope. Atomic force microscopy (AFM) images of the uncapped semicrystalline polymer films were also obtained using an Asylum Research MFP-3D atomic force microscope operating in tapping mode. The AFM images were used to determine the surface area (A_o) of the uncapped PCap and PEO films. As the samples were quite rough, the measured surface area was typically larger than the scan areas used to obtain the images (A_{scan}). A series of AFM images were taken at different positions on each sample and a number of images were collected at each position using scan sizes in the range $10\ \mu\text{m}\times10\ \mu\text{m}$ to $90\ \mu\text{m}\times90\ \mu\text{m}$. Different scan sizes were used at each position so that suitable statistics could be obtained for the measured surface area of the samples and to ensure that this area scaled linearly with the scan areas used. This also enabled us to check that the area values measured were not dependent upon experimental artifacts such as those due to the shape of the AFM tip. Following the preparation of the bilayers, optical micrographs and AFM images of the sample surfaces were collected using the same parameters that were used to image the PEO and PCap layers. The AFM images were also used to determine the surface area of the bilayers (A_1). The value of A_1 was determined at different positions on the sample surfaces by collecting multiple images (using different scan sizes) at each position. As shown in Figs. 2 and 3, the appearance of the bilayers was very similar to that of the uncapped PCap

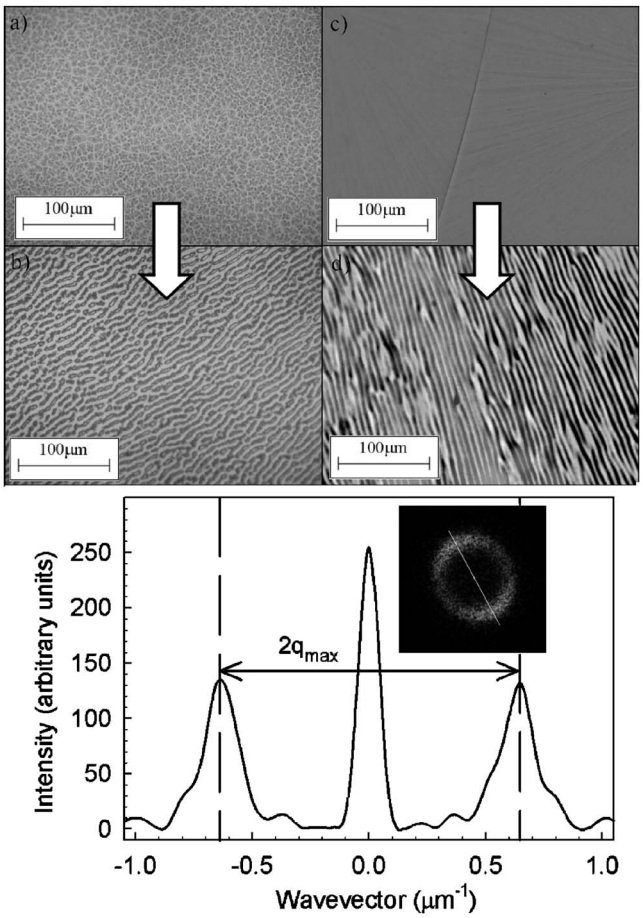

FIG. 2. Optical micrographs of PCap/PS and PEO/PMMA bilayers taken before and immediately after (within 1 s) heating above the melting temperature of the semicrystalline underlayers. Panels (a) and (b) show the surface of PCap/PS bilayer comprising a 107 nm thick PCap underlayer and a 115 nm thick PS capping layer. Panel (a) shows the surface of the bilayer at 25 °C prior to heating and panel (b) shows an image of the same region taken within 1 s of heating the bilayer to 65 °C [T_m(PCap)=58 °C]. Panels (c) and (d) show the surface of PEO/PMMA bilayer comprising a 371 nm thick PEO underlayer and a 118 nm thick PMMA capping layer. Panel (c) shows the surface of this bilayer at 25 °C prior to heating and panel (d) shows an image of the same region taken within 1 s of heating the bilayer to 70 °C [T_m(PEO)=63 °C]. The bottom panel shows a line profile of the radial intensity distribution that was taken from the 2D Fourier transform (FT, see inset in bottom panel) of the image shown in panel (b). This line profile was taken along a line joining the center of the FT and the two dominant peaks on either side of the center of the FT. These line profiles were used to determine the position of the dominant peak in wave-vector space, $q_{\max}$.

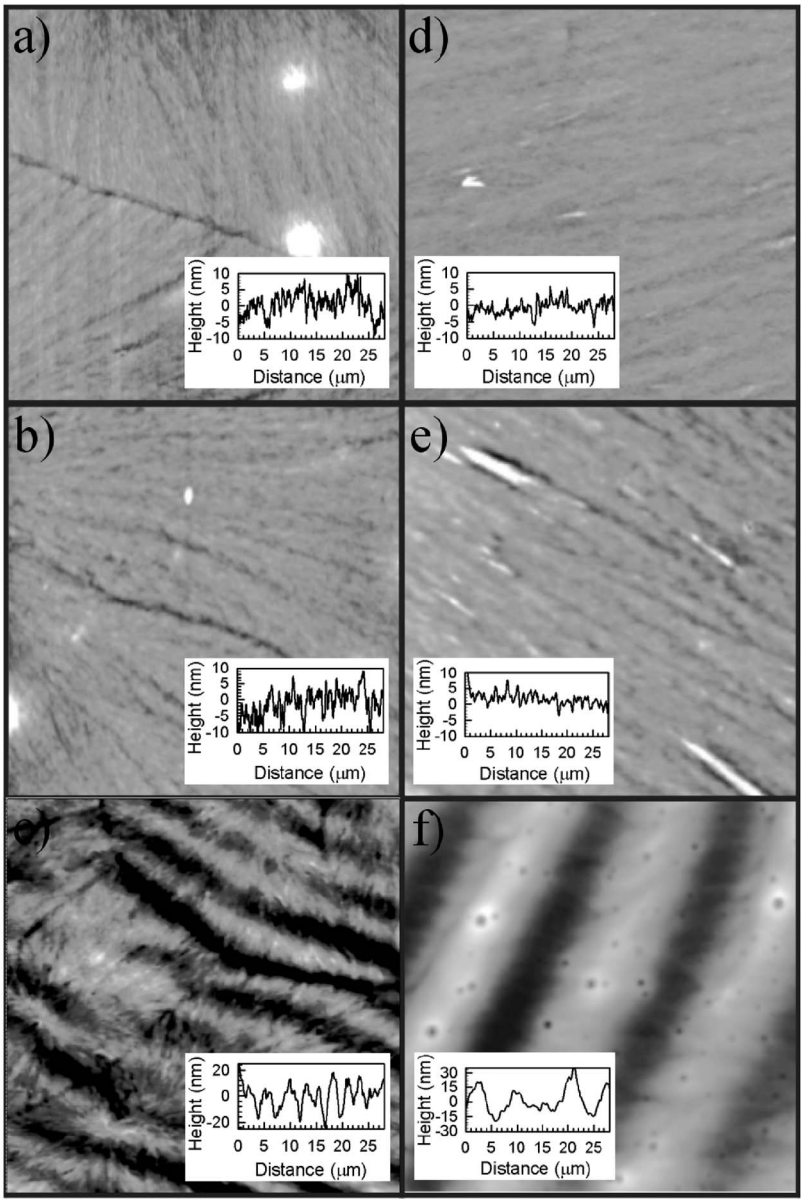

FIG. 3. Atomic force microscope images of PCap and PEO films and PCap/PS and PEO/PMMA bilayers taken before and after heating. Panel (a) shows the surface of a 67 nm thick PCap film prior to bilayer formation. Panel (b) shows the surface of a PCap/PS bilayer that was formed by placing a 47 nm PS capping layer on top of the film shown in panel (a). This image was taken at 25 °C and prior to heating. Panel (c) shows the surface of the same PCap/PS bilayer after heating to 65 °C for ~1 s, followed by a rapid quench (~50 °C min^{-1}) to room temperature. Panel (d) shows the surface of a 174 nm thick PEO film prior to bilayer formation. Panel (e) shows the surface of a PEO/PMMA bilayer that was formed by placing a 70 nm thick PMMA capping layer on top of the film shown in panel (d). This image was taken at 25 °C and prior to heating. Panel (f) shows the surface of the same PEO/PMMA bilayer after heating to 70 °C for ~1 s, followed by a rapid quench (~50 °Cmin^{-1}) to room temperature. All AFM images were collected in tapping mode and were taken using a 20 μm × 20 μm scan area. The insets in all of the panels show a height profile of the surface of the samples that was taken along one of the main diagonals of each image.

and PEO films, respectively, and AFM images of the bilayers revealed that the surface area of the bilayer samples was similar to that of the uncapped semicrystalline polymer films (i.e., $A_1 \approx A_o$). This confirmed that the capping layers had been pulled into intimate contact with the underlayers during bilayer formation.

A range of different bilayer samples having different combinations of the underlayer and capping layer thickness were prepared using the methods described above. All of the bilayer samples were then placed individually onto a Linkam hot stage and mounted on the stage of an Olympus BX51 optical microscope equipped with an Olympus DP70 digital camera and connected to a computer equipped with Image Pro Plus image capture/analysis software (Media Cybernetics). In each case, the bilayer samples were rapidly heated (90 °C min^{-1}) to a temperature, T_{exp}, that was above the melting point of the semicrystalline polymer underlayer, but below the glass transition temperature of the glassy polymer capping layer [T_{exp}(PCap/PS)=60 °C and T_{exp}(PEO/PMMA)=70 °C]. During heating the bilayer samples were observed under bright field illumination using the optical microscope. In each case, when the temperature exceeded the melting temperature of the underlayer, the morphology of the surface of the bilayer changed from something similar to that of the semicrystalline underlayers to having periodic one-dimensional corrugations with a well-defined wavelength [Figs. 2(b) and 2(d)]. The anisotropy in these structures occurs as the result of small stresses that are introduced into the capping layers when they are placed on top of the semicrystalline underlayers using the water transfer techniques described above. As the capping layers were transferred manually onto the surface of the underlayer films, this often resulted in a small amount of tension being applied to the films in one direction while surface forces were pulling the layers into contact. These small anisotropic stresses introduce a preferred direction into the samples that correlates with the breaking of symmetry observed during the wrinkling process. Similarly, small defects or dust particles

in the samples were also shown to act as nucleating sites for the wrinkling process and to introduce a level of anisotropy into the observed wrinkling morphologies. Samples that were prepared in such a way as to minimize the introduction of stresses into the capping layers during bilayer formation produced more isotropic wrinkling morphologies. As can be seen from Figs. 2(b) and 2(d), the level of anisotropy varied from sample to sample. A consideration of the image in Fig. 2(b) shows that while the local anisotropy is quite high in this image, the direction of the anisotropy changes at different positions on the samples. It is this variation in the direction of the anisotropy that gives the ringlike structure that is observed in the Fourier transform shown in the bottom panel of Fig. 2. Images such as the one shown in Fig. 2(d) produce more anisotropic Fourier transforms that have isolated lobes.

Optical micrographs of the bilayer surfaces were collected immediately after the formation of the wrinkles and within <1 s of melting the underlayers (see Fig. 2). This was done because the initial wrinkling wavelength was observed to coarsen with prolonged annealing time. As reported previously, this coarsening was observed to be much faster in bilayer samples with thicker underlayers and thinner capping layers and occurs as the result of the relaxation of residual stresses in the wrinkled capping layers [17]. The optical micrographs of the samples that were obtained shortly after the formation of the corrugations were Fourier transformed (FT) using the Image Pro Plus software. The dominant wave vector ($q_{\max}$) in the images was then determined by taking a line profile that passed through the center of the FT and the first peak on either side of the central intensity maximum (see bottom panel, Fig. 2). The value of $q_{\max}$ corresponding to the position of the first peak maximum was then used to determine the dominant wavelength, λ, of the morphology using the expression $\lambda=2\pi/q_{\max}$. This procedure was repeated for each of the different bilayers studied and for different combinations of the underlayer and capping layer thickness. The results are shown in the plots in Fig. 4.

Following the formation of the surface corrugations, the bilayer samples were rapidly quenched to room temperature by removing them from the hot stage and the semicrystalline underlayers were allowed to recrystallize. The surface of the bilayers was then imaged with an AFM using the same scan parameters that were used to study the bilayers prior to heating. Figure 3 shows examples of AFM images of the different bilayer systems that were collected before and after heating the samples. These images show that it is possible to freeze in the wrinkled surface structure by rapidly quenching the samples and recrystallizing the semicrystalline layer. The line profiles that are shown in this figure illustrate that the structures that are formed at the surface of these samples during heating typically have larger height variations than the roughness observed on the unheated bilayers. However, as shown in Fig. 3 [panel (c)], the underlying roughness that is associated with spherulitic structure of the semicrystalline underlayers can be clearly seen on top of the wrinkled structures when the underlayers are recrystallized.

A final set of bilayer samples were also prepared by placing glassy polymer capping layers on top of molten underlayers at temperatures of 60 and 70 °C for the PCap/PS and PEO/PMMA bilayers, respectively. Samples that were produced in this way did not show the wrinkling behavior described above. These simple experiments illustrate that it is the process of melting the semicrystalline underlayer that is responsible for driving the wrinkling transition at the surface of the bilayers. These tests also rule out the possibility of dispersion driven forces being responsible for the wrinkling [5]. If dispersion effects were significant in the samples being studied, then they would cause the wrinkling to occur even when the underlayers are in the molten state.

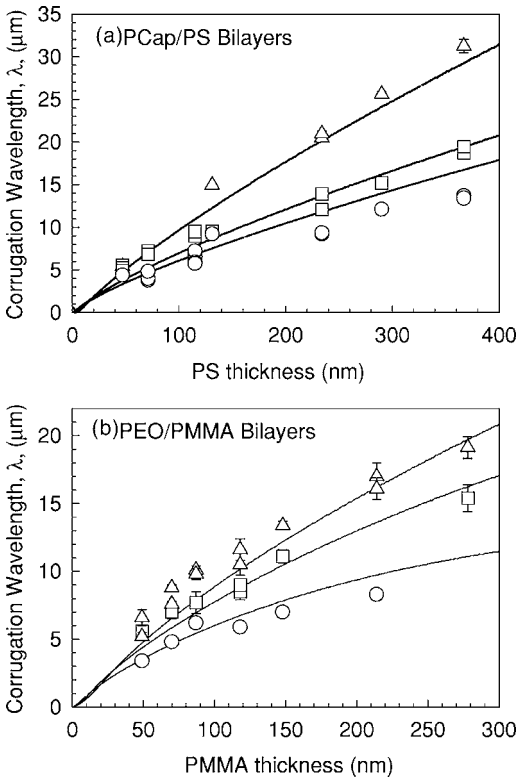

FIG. 4. Characteristic wavelength of the wrinkling morphology for each of the bilayer samples studied. Data are shown as function of the capping layer thickness (L) for different values of the underlayer thickness (h_o). The experimental data were obtained from values of $q_{\max}$ that were determined from FT line profiles (similar to those shown in Fig. 2), using the relation $\lambda=2\pi/q_{\max}$. Panel (a) shows data that were collected from thin film PCap/PS bilayer samples where the thickness (h_o) of the underlying PCap film was 67 nm (○), 107 nm (□), and 462 nm (Δ), respectively. Panel (b) shows data that were collected from thin film PEO/PMMA bilayer samples where the thickness (h_o) of the underlying PEO film was 174 nm (○), 371 nm (□), and 650 nm (Δ) respectively. The solid lines in this figure represent values of the fastest growing wavelength that were calculated from simulations of the amplitude growth rate, $s(q)$, that were determined using Eq. (9). The values of E, G, ν_L, and ϵ that were used to generate these lines are given in Table I.

Measurements of the frequency-dependent shear modulus $[G(\omega)=G'(\omega)+iG''(\omega)]$ of poly(caprolactone) ($M_w=10\,000$ gmol^{-1}, *Sigma*) and poly(ethylene oxide) ($M_w=35\,000$ gmol^{-1}, *Sigma*) were taken using a parallel plate rheometer (Anton Parr MCR 301) operating over a range of frequencies from 0.1 to 600 rad s^{-1}. The values of $G(\omega)$ were determined at temperatures, T_{Rheo}, just above the melt-

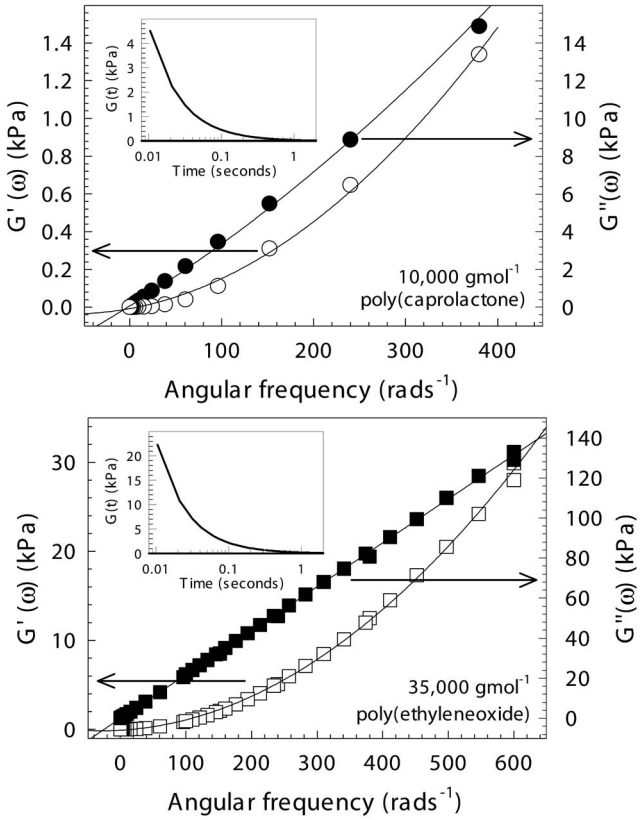

FIG. 5. Frequency dependence of the shear modulus of a 10 000 $gmol^{-1}$ poly(caprolactone) sample taken at 60 °C (top panel) and a 35 000 $gmol^{-1}$ poly(ethylene oxide) sample (bottom panel) taken at 65 °C. Hollow and filled symbols are used to represent the real and imaginary parts [$G'(\omega)$ and $G''(\omega)$] of the frequency-dependent modulus, respectively. The arrows point to the axis that is related to each data set. The solid lines shown on these plots are the results of polynomial fits to the $G'(\omega)$ and $G''(\omega)$ data. The insets in each panel show the time-dependent stress relaxation modulus of the polymers. These plots were obtained by Fourier transformation of the frequency-dependent modulus $[G(\omega)=G'(\omega)+iG''(\omega)]$ of the polymers that were constructed using the polynomial fits to the frequency-dependent rheology data.

ing temperature of the polymers [$T_{\mathrm{Rheo}}(\mathrm{PCap})=60$ °C and $T_{\mathrm{Rheo}}(\mathrm{PEO})=65$ °C] in the presence of an inert nitrogen atmosphere and using typical strains of ~1%. Polynomial fits were then made to the $G'(\omega)$ and $G''(\omega)$ data over the range of frequencies studied (see Fig. 5). These fits were then used to construct the complex frequency-dependent shear modulus $G(\omega)=G'(\omega)+iG''(\omega)$. This was then Fourier transformed to obtain the time-dependent stress relaxation modulus $[G(t)]$ for each of the polymers studied (see insets, Fig. 5).

III. RESULTS AND DISCUSSION

Figures 2 and 3 show that the morphology of the structures that are present on the surface of the bilayers prior to heating are similar to those that are associated with the spherulitic structure of the uncapped semicrystalline polymer films. However, these figures also show that there are large differences in the spherulitic structure (and corresponding roughness) of the underlying semicrystalline polymers films that are used to form each type of bilayer sample studied [see Figs. 2(a) and 2(c)].

The structures that form after heating the samples are similar in appearance for both types of bilayer studied. However, the length scales associated with the wrinkling are different in each case (see Fig. 4). As described previously [17], wrinkle formation at the bilayer surface is driven by the reduction of the interfacial area between the semicrystalline underlayer and the glassy polymer capping layer that occurs when the underlayer is melted. When the underlayers melt, interfacial tension acts to minimize the total interfacial area and remove the excess roughness associated with spherulitic structure of this layer. As the glassy polymer capping layers are in intimate contact with the underlayer, the melting of the underlayer pulls the interface between the two layers flat and reduces the area of the capping layer. The capping layers therefore have their total area reduced from something that is close to the surface area of the semicrystalline underlayers (prior to heating) to having an area that is equal to their projected area on the substrate after heating. This reduction in area leaves the glassy polymer capping layers in a state of compressive stress [see Fig. 1(d)]. Thermal fluctuations at the surface of the bilayers then cause the capping layers to buckle so that the system can release excess strain energy. The surface of the capping layer is prevented from buckling with the lowest energy bending mode (i.e., with a large wavelength) because of kinetic constraints that are placed on the system due to the need to transport material in the molten underlayers. The intimate contact between the two layers, and the requirement that material in the underlayer is conserved, forces the buckling process to select a characteristic wrinkling wavelength that represents a compromise between the initial in-plane stresses in the films, the bending stresses in the wrinkled capping layers, and the stresses that evolve in the viscoelastic molten underlayers [17] [Fig. 1(e)]. However, any anisotropic residual stresses that remain in the samples following bilayer preparation will cause the wrinkling to occur in one dimension. The reason for this is that wrinkling in one dimension requires less bending energy to be stored in the films than in the case of two-dimensional wrinkling (for a given perturbation wavelength). As a result of this, the presence of even a small anisotropy in the stresses in the capping layer will cause symmetry breaking in this system and the wrinkling process will produce one-dimensional surface corrugations. As mentioned above, if great care is taken to reduce the anisotropy of the residual stresses that are introduced into the capping layers during bilayer formation, more isotropic wrinkling structures can be observed.

In the following section, we derive an expression that considers the balance of forces that are exerted on the glassy capping layers during the melting of the semicrystalline underlayers. This simple model describes how fluctuations at the surface of the bilayers with a particular wave vector, q, evolve with time. It is shown that the amplitude growth rate, s, is q-dependent and that there exists a particular wave vector q_{max} for which amplitude fluctuations are expected to grow faster than for all other wave vectors. The results of

this simple model are used to predict the dominant wrinkling wavelength for this system and the results of the calculations are compared to experimental data obtained for the initial wrinkling wavelengths in the bilayers studied. We show that this model can be used to quantitatively predict the wrinkling length scales for the bilayers studied here, if the thickness and mechanical properties of the films that comprise the bilayers are known.

A. Wrinkling model

In modeling the mechanism responsible for the formation of the wrinkles at the surface of the bilayers, we consider the two layers separately. In all that follows, we will simplify the problem by assuming that the wrinkling occurs in only one dimension. We begin by considering the flow of material in the molten semicrystalline polymer underlayers when they are subjected to small spatial variations in the surface pressure, $P_z(x)$ [see Fig. 1(e)]. A consideration of the flux of material in this layer and the assumption that material is conserved gives rise to the continuity equation

$$\frac{dh}{dt} = \frac{h^3}{3\eta}\frac{d^2P_z}{dx^2}, \tag{1}$$

where h and η are the thickness and viscosity of the molten semicrystalline underlayer, respectively. The form of the spatially varying surface pressure $P_z(x)$ can be constructed by considering the balance between the z components of the forces that act on the glassy polymer capping layer and results in an expression of the form [17]

$$P_z(x) = E\epsilon L\frac{d^2h}{dx^2} + \frac{EL^3}{12(1-\nu_L^2)}\frac{d^4h}{dx^4} - \sigma_{zz}, \tag{2}$$

where E, ν_L, and L are Young's modulus, the Poisson ratio, and the thickness of the glassy polymer capping layer, respectively, and ϵ is the strain introduced into the capping layers by the reduction in area of the interface between the two layers. The first term in this expression represents the normal component of the stresses that occur due to the strain in the glassy polymer capping layers, which have an out-of-plane component when the capping layer starts to buckle [21]. The second term describes the out-of-plane component of the surface pressure that is caused by the bending of the capping layer during wrinkling [21], and the third term, σ_{zz}, accounts for the pressure that is exerted on the glassy polymer capping layers due to the elastic component of the response of the viscoelastic underlayers [8,9].

Equation (2) also describes spatial variations in the fluctuation in pressure at the interface between the two polymer layers. The difference between the first two terms and the third term in this equation, therefore, describes the net downward pressure exerted on the underlayer by the elastic capping layer during the initial stages of wrinkling. If the restoring force provided by the underlayer were equal and opposite to the downward force exerted by the elastic film at all times during the wrinkling process, then the film would remain flat and wrinkling of the capping layers would not occur. In the initial stages of wrinkling, small spatial fluctuations in the vertical component of the pressure must exist to drive wrinkle formation. Equation (2) assumes that these small deviations give rise to nonzero, spatially varying pressure fluctuations $P_z(x)$ at the surface of the bilayer that drive the initial wrinkling process and result in the selection of the characteristic wavelength in the system.

An approximation to the form of σ_{zz} used in Eq. (2) can be derived by using a method similar to that used by Fredrickson *et al.* [22] and Yoo and co-workers [8,9,13]. This method considers the mechanical response of an elastic layer that is subjected to sinusoidal surface perturbation of the form $h(x)=h_o+A(t)\cos(qx)$, where h_o is the average thickness of the molten underlayer and $A(t)$ is the time-dependent amplitude of a disturbance of wave vector, q. We assume that all deformations in the underlayer are small and use the tensor form of Hooke's law,

$$\sigma_{ik} = K\delta_{ik}u_{ll} + 2G\left(u_{ik} - \tfrac{1}{3}u_{ll}\right), \tag{3}$$

to relate the stress to the strain fields, u_{ik}, in the underlayer [23]. In this expression, δ_{ik} is the Kronecker delta, K and G are the compressibility and shear moduli of the viscoelastic underlayer, respectively, and $(x_1,x_2)=(x,z)$.

The strain fields, u_{ik}, are then calculated from the displacement fields, u_i, using the expression [23]

$$u_{ik} = \frac{1}{2}\left(\frac{\partial u_i}{\partial x_k} + \frac{\partial u_k}{\partial x_i}\right). \tag{4}$$

We then proceed according to the method adopted by Yoo and co-workers [13] and assume that the viscoelastic layer is subject to the required sinusoidal surface perturbation with periodic boundary conditions in the horizontal direction. We also assume that there is no tangential component of the stress at the surface of the viscoelastic underlayer and that $\frac{\partial\sigma_{ik}}{\partial x_k}=0$. The displacement fields (u_x and u_z) can then be written in the form

$$u_x = u_1 = A(t)\psi_1(z)\sin(qx),$$

$$u_z = u_2 = A(t)\psi_2(z)\cos(qx), \tag{5}$$

where $\psi_1(z)=C_1[\sinh(qz)+qz\cosh(qz)]+C_2qz\sinh(qz)$ and $\psi_2(z)=C_2[\sinh(qz)-qz\cosh(qz)]-C_1qz\sinh(qz)$. The coefficients $C_1(qh_o)$ and $C_2(qh_o)$ are given by the form [22]

$$C_1(qh_o) = \frac{qh_o\cosh(qh_o)}{qh_o - \sinh(qh_o)\cosh(qh_o)},$$

$$C_2(qh_o) = \frac{\cosh(qh_o) + qh_o\sinh(qh_o)}{qh_o - \sinh(qh_o)\cosh(qh_o)}. \tag{6}$$

Combining Eqs. (3)–(6) with the required boundary conditions gives the following result for the normal component of the stress exerted on the glassy capping layer due to the elastic component of the response of the underlayer, σ_{zz}:

$$\sigma_{zz}(x,h_o,t) = 2qGA(t)\cos(qx) \times\left(\frac{qh_o\sinh(2qh_o)+(qh_o)^2[2\cosh^2(qh_o)-1]}{\sinh(qh_o)\cosh(qh_o)-qh_o}\right). \tag{7}$$

Inserting Eq. (2) into Eq. (1) gives an expression that describes the time-dependent evolution of amplitude/height fluctuations at the surface of the bilayer. Assuming that the amplitude displacements, $A(t)$, are small in comparison to the thickness of the underlayer at early times, the resulting expression can be linearized to give

$$\frac{dh}{dt} = \frac{h_o^3}{3\eta}\left(E\epsilon L\frac{d^4h}{dx^4} + \frac{EL^3}{12(1-\nu_L^2)}\frac{d^6h}{dx^6} - \frac{d^2\sigma_{zz}}{dx^2}\right). \tag{8}$$

Inserting the result of Eq. (7) and using a trial solution, $h(x,t)=h_o+A(t)\cos(qx)$, gives an equation of the form $\frac{dA(t)}{dt} = s(q)A(t)$, where the growth rate $s(q)$ has the form

$$s(q) = \frac{h_o^3}{3\eta}\left[E\epsilon Lq^4 - \frac{EL^3}{12(1-\nu_L^2)}q^6 + 2Gq^3\left(\frac{qh_o\sinh(2qh_o)+(qh_o)^2[2\cosh^2(qh_o)-1]}{\sinh(qh_o)\cosh(qh_o)-qh_o}\right)\right]. \tag{9}$$

We note at this point that the expression given above is only valid in the initial stages of wrinkling. The model described above is therefore only capable of predicting the response of the system during the period where the initial wavelength is selected. It is incapable of predicting the time evolution of the wrinkling morphology after the initial wrinkle formation has occurred.

The use of the shear modulus G in Eq. (9) requires some interpretation at this point. In making the transition from the case of an elastic material to a viscoelastic one, we must be careful in interpreting and using the value of G as it is defined above. A comparison of the values of the early time stress relaxation modulus of the underlayer materials obtained in the present study (~5–30 kPa, see Fig. 5) with typical values of the relaxation modulus of glass forming polymers (see Fig. 7 of Ref. [16] and Ref. [20]) shows that the underlayers are not glassy on these short time scales ($G_{\text{glass}}\sim 1$ GPa). Moreover, the time dependence of the stress relaxation modulus in these materials is consistent with that of the viscoelastic response of an uncrosslinked, low molecular weight polymeric liquid and $G(t)$ is therefore expected to be a time-dependent quantity for these materials. In the present model, we assume that the value of G in Eq. (9) represents an effective average value of the early time value of the stress relaxation modulus $G(t)$. In a previous study [17], the value of G that was used to fit the data was found to be approximately the same as the value of $G(t)$ taken at a time of ~0.01 s. If we adopt the same approach in the present work, a comparison with the insets shown in Fig. 5 suggests that values of G(PCap) ~ 5 kPa and G(PEO) ~ 24 kPa are appropriate values for the stress relaxation modulus of the underlayer materials used here. We note at this stage that the optical micrographs of the wrinkling bilayers were obtained on experimental time scales of up to ~1 s. However, this should be viewed as a generous upper bound on the time at which the micrographs were collected relative to formation of the wrinkles. In principle, the images of the sample surfaces were collected as soon as the wrinkles had formed, but reaction times and the response of experimental equipment were found to take a finite amount of time. Clearly, a response time of ~0.01 s is unlikely to be achieved in these experiments, but a time averaged value of G evaluated at a time of 0.01 s does not seem unrealistic in the context of the present model.

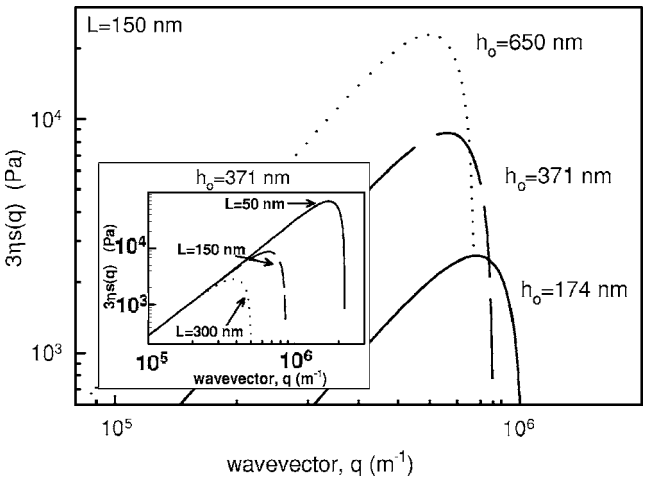

FIG. 6. Calculations of the q-dependant growth rate $[3\eta s(q)]$ for sinusoidal perturbations at the surface of the bilayers studied. The main panel shows calculations of the reduced growth rate for a fixed value of the capping layer thickness (L=150 nm) using values of h_o=174, 371, and 650 nm, respectively. The inset shows the results of similar calculations that were performed for a fixed value of the underlayer thickness (h_o=371 nm) using different values of L=50, 150, and 300 nm, respectively. All of the curves shown are calculated using Eq. (9) with values of E=3.7 GPa, ν_L=0.325, $\epsilon = 0.1\times10^{-3}$, and G=24 kPa, respectively.

Figure 6 shows plots of the reduced growth rate $3\eta s(q)$ that were obtained using Eq. (9) for different values of the thickness of the capping layer (L) and underlayer (h_o), respectively. For values of $s(q)<0$, fluctuations at the surface of the film will be suppressed. However, when $s(q)>0$ these fluctuations will be amplified. As shown in Fig. 6, $s(q)$ has a well-defined maximum at a wave vector $q_{\max}$. Surface corrugations with this wave vector will grow exponentially faster than all other fluctuations and are expected to dominate the morphology at the surface of the bilayers at early times. Figure 6 also shows that the growth rate of fluctuations at the surface of the bilayers is larger in samples with thicker underlayers (large h_o) and thin capping layers (small L). This is consistent with the experimental observation that the wrinkling morphology coarsens faster in bilayers with large values of h_o and smaller values of L.

B. Comparison between the model and results

Plots similar to those shown in Fig. 6 were used to determine the wave vector $q_{\max}$ with the largest growth rate, for

TABLE I. Bilayer material parameters used in the calculation of the wave-vector-dependent amplitude growth rates, $s(q)$ [see Eq. (9)].

Parameter	PCap/PS bilayer	PEO/PMMA bilayer
E (GPa)	3.4 [20]	3.7 [20]
G (kPa)	5.0±1.5	24.0±2.0
ν_L	0.325 [20]	0.325 [20]
ϵ	$(0.35\pm0.05)\times10^{-3}$	$(0.1\pm0.05)\times10^{-3}$

different values of the underlayer and capping layer thickness. In each case, the value of the underlayer thickness h_o was fixed at the value of the experimentally determined underlayer thickness and the capping layer thickness was increased incrementally. Values of $q_{\max}$ were then calculated for each value of the capping layer thickness using the condition that $\frac{ds}{dq}(q_{\max})=0$. The values of $q_{\max}$ obtained using this method were then used to calculate the characteristic wavelength, λ, of the wrinkling morphology at early times using the expression $\lambda=2\pi/q_{\max}$. The solid lines in Fig. 4 show the results of calculations that were performed for both the PCap/PS and PEO/PMMA bilayers studied. Table I lists the parameters that were used to calculate the solid lines shown in this figure. Values of G were extracted from the rheological measurements of PEO and PCap shown in Fig. 5 (as described above) and values of the Poisson ratio (ν) and Young's moduli (E) of the capping layers were obtained from the literature [20].

The values of the strain (ϵ) that were used in the calculations were determined from the AFM images of the bilayer surfaces. Prior to heating, the surface area of the capping layers was assumed to be equal to the value of the area measured using the AFM (A_1). After heating and the subsequent melting of the underlayers, the polymer/polymer interface was assumed to be pulled completely flat and the resulting area was assumed to be comparable to the projected area of the film on the substrate. In the case of the individual AFM images that were used to determine the surface area of the samples prior to heating, this corresponds to the scan area that was used to collect each image. The values of A_1 and the corresponding scan areas (A_{scan}) obtained from each image were then used to calculate the effective linear strain, ϵ, introduced into the capping layers by melting the semicrystalline underlayers using the expression $\epsilon\approx\frac{A_1-A_{\text{scan}}}{2A_{\text{scan}}}$. Values of the strain that were determined using this method were found to be consistent for each set of bilayers studied.

It is worth commenting about the validity of the assumptions used in determining the strain at this stage as this assumes that the capping layers are in a state of zero stress prior to heating the bilayers. When the capping layers are placed on top of the semicrystalline films, the glassy polymer membranes would be forced to increase their total area in order to conform to the underlayer surface. This would mean that melting of the underlayer would simply relax any stresses that are introduced by the sample preparation procedure and would cause the contraction of the capping layers back to a state of zero stress and the wrinkling process would not occur. So how can the capping layers be in a state of zero (or close to zero) stress prior to melting the underlayers? There are two possible reasons why this could occur. Either the production of the bilayers results in the yield and flow of the capping layer as the two layers are pulled into contact, or there is sufficient slack in the free-standing membranes that are used to form the capping layers to compensate for the increase in contour length of these layers during bilayer formation [17]. Yield of the capping layers would leave them in a stress-free state, but this seems unlikely. This is because the typical strains associated with the change in the area of the free-standing membranes that occur during bilayer formation are of the order of $(0.1-0.35)\times10^{-3}$ (as determined from AFM images of the uncapped underlayer surfaces). A simple calculation of the stresses involved in increasing the area of the initially flat capping layer membranes ($\sigma_{\text{prep}}=E\epsilon$) gives an upper bound of $\sigma_{\text{prep}}\sim1.2$ MPa. This is an order of magnitude smaller than the stresses that are required to cause the onset of nonlinear mechanical processes in similar glassy polymers ($\sigma_{\text{yield}}\sim30$ MPa, $\epsilon_{\text{yield}}\sim0.01$) [25]. The possibility of having excess slack in the free-standing membranes that were used to form the capping layers seems more likely. Despite the fact that these films were annealed above a hot plate to remove short wavelength wrinkles in the membranes and to tighten them (prior to bilayer formation), sufficient excess area could have existed in the free standing membranes to allow the capping layers to conform to the surface of the semicrystalline layer. The reason for this is that the annealing process removes short wavelength wrinkles very quickly while the removal of slack in the supported films requires much longer times because of the need to transport material over larger distances. Both of these effects provide possible explanations as to how the capping layers can be in a stress free state prior to heating the bilayers, but they are difficult to quantify in the context of the present experiments.

The data shown in Fig. 4 indicate that the wavelength of the morphology is sensitive to the molecular weight (and hence the mechanical properties) of the underlayer, as can be expected from Eq. (9). This can also be confirmed by comparing the results shown in the bottom panel of Fig. 4 with those obtained in our previous study on PEO/PS bilayers that used a lower molecular weight PEO underlayer [17]. The mechanical properties of the capping layers used in all three bilayer systems are expected to be very similar at the temperatures studied [20]. As the molecular weight of the underlayer is increased, the wavelength of the wrinkling morphology is expected to be reduced for a given set of values of h_o and L according to Eq. (9). This can be interpreted in the following way. As the molecular weight of the polymer used in the underlayer is increased this causes a corresponding increase in the value of G. This means that for a deformation in the underlayer of a given size, there will be an associated increase in the strain energy stored in the films. The result of increasing G is therefore to suppress large deformations such as those caused by long-wavelength (small q) surface perturbations and to shift the dominant wrinkling wavelength to smaller values. The reduction in the wrinkling wavelength that is observed for the PEO/PMMA bilayers shown in Fig. 4 is particularly significant given the differences in the size of the strains that are driving the wrinkling of the capping lay-

ers. As can be seen from Fig. 3, the surface area of the PCap/PS bilayers prior to heating is typically larger that of the corresponding PEO/PMMA bilayers. This results in a much lower final strain being introduced into the PMMA ($\epsilon=0.10\pm0.05\times10^{-3}$) capping layers than in the case of the PS capping layers ($\epsilon=0.35\pm0.05\times10^{-3}$). These values are also smaller than the strains that were found in our previous study of PEO/PS bilayers [17]. According to calculations based on Eq. (9), reducing the strain in the capping layer is expected to increase the wrinkling wavelength. This means that the effects due to increasing the stiffness of the polymer underlayer dominate over effects due to the reduced strain in the capping layers for the PEO/PMMA bilayers studied here, resulting in a reduced wrinkling wavelength in these bilayers.

Figure 4 also illustrates that the analytical form of the growth rates derived in Eq. (9) accurately predicts the characteristic wrinkling wavelengths that form in this system. This is surprising given that the viscoelastic properties of the underlayer materials were represented by inserting the results for the response of an elastic layer [Eq. (7)] into an equation describing the viscous flow in the underlayers [Eq. (1)]. Moreover, the form of Eq. (1) assumes that the flow in the underlayers is incompressible. These are clearly rather crude approximations to the true viscoelastic response of the underlayers. A more detailed and rigorous analysis of the wrinkling of an elastic layer supported on a viscoelastic underlayer can be found in recent theoretical studies by Huang and co-workers [16,26]. Despite the limitations of the model described in the present work, the initial wrinkle wavelengths that are predicted using Eq. (9) are shown to be in good agreement with experimental data with only a few small discrepancies being observed. The reason why the elastic and viscous components of the underlayer response can be decoupled in the model used here is not clear at this stage. One possible explanation could be related to the range of viscosities and the elastic moduli associated with the response of these materials. Typical values for the viscosity of the underlayers can be obtained directly from the slope of the $G''(\omega)$ versus ω plots shown in Fig. 5 [24]. A consideration of these plots shows that the viscosity of the PCap and PEO used in this study are $\sim$0.039 and $\sim$0.215 Pa s, respectively, and that the frequency-dependent storage modulus $[G'(\omega)]$ of the materials varies in the range 0–140 kPa. As these materials are relatively soft, there may be some decoupling of their elastic and viscous properties, although this is difficult to quantify in the context of the present study.

The fits shown in Fig. 4 illustrate that the model proposed in the current work correctly captures the both the underlayer and capping layer thickness dependencies of the initial wrinkling wavelength and suggests that the proposed mechanism for wrinkle formation is the correct one. An encouraging aspect of the work presented here is that the values of G that were predicted above based upon the results of our previous analysis [17] (also see Table I) were able to accurately describe the data shown in Fig. 4. However, some deviation from the fits can be observed for the thinnest underlayers in the PCap/PS bilayers. It is unclear why the model deviates from the experimental data for these samples. One possible cause for the extra curvature at large values of L, could be due the onset of the effects of dispersion driven forces for these thinner underlayer films. However, the addition of a dispersion term of the form $\frac{h_o^3}{3\eta}\frac{Aq^2}{2\pi(h_o+L)^4}$ [8,9] (where $A\sim1\times10^{-19}$ J [27]) to the right-hand side of Eq. (9) makes no difference to the shape of the calculated curves.

Another source of these discrepancies could be caused by changes in the area of the polymer/polymer interface during the wrinkling process. As the wrinkles form, the interfacial area between the two layers might be expected to increase slightly as the initially flat, strained capping layers are deflected out of the plane of the sample surface. However, the model described above is only valid in the limit of small deflections of the capping layer. The changes that occur in the area of the polymer/polymer interface due to the growth of the amplitude of the wrinkles during this initial period are likely to be small. If these small increases in the interfacial area did play a significant role in selecting the initial wavelength, they could be accounted for by including an additional term of the form $\gamma_i\frac{d^2h}{dx^2}$ on the right-hand side of Eq. (2) (where γ_i is the interfacial tension of the two polymers). This would mean that the coefficient of the second derivative in Eq. (2) [and the corresponding q^4 term in Eq. (9)] would become $E\epsilon L-\gamma_i$. Inserting typical values of $E=3.4$ GPa, $\epsilon=0.35\times10^{-3}$, $L=200$ nm, and $\gamma_i=4$ mJ m^{-2} [20] we find that the addition of the interfacial tension term causes a change in this coefficient of only $\sim$1% and its inclusion in the model makes no discernible difference to the shape of the calculated lines shown in Fig. 4. However, we note that in the case of very thin underlayer films ($\sim$10 nm thick) both dispersion forces and effects due to the changing interfacial area between the two polymers will become significant. In this case, both a dispersion term and an interfacial energy term should be added to Eqs. (2) and (9).

An additional concern related to the role played by interfacial effects arises if the elastic energy stored in the capping layers is greater than the work of adhesion between the two polymer layers [10]. In this case some of the stored strain energy could be used to overcome the adhesive interactions between the two polymer surfaces and a degree of interfacial failure could occur. If we consider the elastic energy that is stored per unit area in the capping layers (U_{strain}) when they experience a strain, ϵ, we obtain an expression of the form $U_{\text{strain}}=\frac{1}{2}EL\epsilon^2$, where E and L are the Young's modulus and thickness of the capping layer, respectively. Inserting typical values of E and ϵ for the capping layers studied in the present work and assuming the maximum film thickness, $L\sim400$ nm, we obtain an upper bound of $U_{\text{srain,max}}=0.1$ mJ m^{-2}. Typical values for the surface tension of the polymers used in these experiments are $\gamma_{\text{surf}}\sim40$ mJ m^{-2}. The work of adhesion (W_{ad}) per unit area between the two polymer layers can then be approximated by the expression $W_{\text{ad}}\sim2\gamma_{\text{surf}}-\gamma_i\sim76$ mJ m^{-2}. This means that $U_{\text{strain,max}}\ll W_{\text{ad}}$ and failure of the interface between the two polymers is unlikely to occur. This suggests that the two layers would remain in intimate contact during the entire wrinkling process.

Another possible explanation for the small discrepancies between the predictions of the model and the data shown in Fig. 4 could be related to the influence of substrate/

interfacial effects on the material properties of these thin polymer layers. Numerous studies have been performed on thin supported films that suggest that free surface and substrate effects can significantly change properties such as the glass transition temperature of ultrathin polymer films [28–30]. The thickness of the thinnest PCap films (67 nm) is comparable to the thickness (~40 nm) where thin film and interfacial effects have been shown to influence the material properties of polymers [28–30]. The role played by the interaction between the PCap films and the native silicon oxide coating on the silicon wafers that were used as substrates could be responsible for stiffening the underlayer. This would give rise to shorter wavelengths than those predicted by the simple theory proposed here. However, these effects are difficult to quantify in the absence of a detailed study of the thickness dependence of the mechanical properties of ultrathin PCap films supported on Si substrates.

IV. CONCLUSIONS

We have described a mechanically driven wrinkling instability in thin film poly(caprolactone)/polystyrene and poly(ethylene oxide)/poly(methyl methacrylate) bilayers. This instability was shown to be driven by changes in the interfacial area between a semicrystalline polymer underlayer and a glassy polymer capping layer that occur when the underlayer is melted. The wrinkling instability was shown to result in the formation of periodic one dimensional corrugations at the surface of the bilayers that have a well-defined wrinkling wavelength on the micron length scale. In both sets of bilayers studied, the initial wrinkling wavelength was shown to depend upon the thickness and mechanical properties of the films that were used to manufacture the samples. A simple model that considered the flow and deformation of material in the molten semicrystalline underlayers and the balance of stresses in the capping layers was used to derive an expression for the wave-vector-dependent growth rates of fluctuations at the sample surface. This model was based upon a linear stability analysis and predicted that the amplitude of fluctuations with a particular wavelength would grow faster than all others. The model was then used to calculate the fastest growing wavelength in this system. It was shown that this simple model can be used to quantitatively predict the characteristic wavelength of the wrinkling instability if the thickness and mechanical properties of the two layers are known.

ACKNOWLEDGMENTS

We thank Professor K. Shakesheff and Professor S. Howdle for providing access to the rheometer that was used in this study. We would also like to thank the Engineering and Physical Sciences Research Council (EPSRC, UK) and the PATTERNS Marie Curie Research Training Network (MRTN-CT-2004-005728, EU Framework Programme 6) for providing funding for this work.

[1] Y. Xia, J. A. Rogers, K. E. Paul, and G. M. Whitesides, Chem. Rev. (Washington, D.C.) **99**, 1823 (1999).
[2] T. Lee, O. Mitrofanov and J. W. P. Hsu, Adv. Funct. Mater. **15**, 1683 (2005).
[3] A. Khademhosseini, R. Langer, J. Borenstein, and J. P. Vacanti, Proc. Natl. Acad. Sci. U.S.A. **103**, 2480 (2006).
[4] A. M. Higgins and R. A. L. Jones, Nature (London) **404**, 476 (2000).
[5] K. Dalnoki-Veress, B. G. Nickel, and J. R. Dutcher, Phys. Rev. Lett. **82**, 1486 (1999).
[6] E. Schäffer, T. Thurn-Albrecht, T. P. Russell, and U. Steiner, Nature (London) **403**, 874 (2000).
[7] N. Bowden, S. Brittain, A. G. Evans, J. W. Hutchinson, and G. Whitesides, Nature (London) **393**, 146 (1998).
[8] P. J. Yoo and H. H. Lee, Phys. Rev. Lett. **91**, 154502 (2003).
[9] P. J. Yoo, K. Y. Suh, H. Kang, and H. H. Lee, Phys. Rev. Lett. **93**, 034301 (2004).
[10] J. S. Sharp and R. A. L. Jones, Phys. Rev. E **66**, 011801 (2002).
[11] J. S. Sharp and R. A. L. Jones, Adv. Mater. (Weinheim, Ger.) **14**, 799 (2002).
[12] H. G. Allen, *Analysis and Design of Structural Sandwich Panels* (Pergamon, Oxford, 1969).
[13] P. J. Yoo and H. H. Lee, Macromolecules **38**, 2820 (2005).
[14] R. Huang and Z. Suo, Int. J. Solids Struct. **39**, 1791 (2002).
[15] N. Sridhar, D. J. Srolovitz, and Z. Suo, Appl. Phys. Lett. **78**, 2482 (2001).
[16] R. Huang, J. Mech. Phys. Solids **53**, 63 (2005).
[17] J. S. Sharp *et al.*, Eur. Phys. J. E **19**, 423 (2006).
[18] R. M. A. Azzam and N. M. Bashara, *Ellipsometry and Polarized Light* (North-Holland, Amsterdam, 1987).
[19] J. A. Forrest, K. Dalnoki-Veress, and J. R. Dutcher, Phys. Rev. E **56**, 5705 (1997).
[20] *Polymer Handbook*, 4th ed., edited by J. Brandrup and E. H. Immergut (Wiley, Hoboken, New Jersey, 1989).
[21] L. G. Jaeger, *Elementary Theory of Elastic Plates* (Pergamon, Oxford, 1964).
[22] G. H. Fredrickson, A. Ajdari, L. Leibler, and J. Carton, Macromolecules **25**, 2882 (1992).
[23] L. D. Landau and E. M. Lifschitz, *Theory of Elasticity*, 3rd ed. (Pergamon, Oxford, 1986).
[24] J. D. Ferry, *Viscoelastic Properties of Polymers*, 3rd ed. (Wiley, Toronto, 1980).
[25] G. Strobl, *The Physics of Polymers*, 2nd ed. (Springer, Berlin, 1997), p. 351.
[26] S. H. Im and R. Huang, J. Appl. Mech. **72**, 955 (2005).
[27] J. Israelachvili, *Intermolecular and Surface Forces*, 2nd ed. (Academic, London, 1991).
[28] J. A. Forrest and K. Dalnoki-Veress, Adv. Colloid Interface Sci. **94**, 167 (2001).
[29] J. S. Sharp and J. A. Forrest, Phys. Rev. Lett. **91**, 235701 (2003).
[30] J. S. Sharp and J. A. Forrest, Phys. Rev. E **67**, 031805 (2003).